



HAL
open science

Effect of an electric field on ferroelectric and piezoelectric properties of brownmillerite $\text{Ca}_2\text{Al}_2\text{O}_5$

R. Arras, C. Paillard, L. Bellaïche

► **To cite this version:**

R. Arras, C. Paillard, L. Bellaïche. Effect of an electric field on ferroelectric and piezoelectric properties of brownmillerite $\text{Ca}_2\text{Al}_2\text{O}_5$. *Physical Review B*, 2023, 107 (14), pp.144107. 10.1103/PhysRevB.107.144107 . hal-04158759

HAL Id: hal-04158759

<https://centralesupelec.hal.science/hal-04158759>

Submitted on 13 Jul 2023

HAL is a multi-disciplinary open access archive for the deposit and dissemination of scientific research documents, whether they are published or not. The documents may come from teaching and research institutions in France or abroad, or from public or private research centers.

L'archive ouverte pluridisciplinaire **HAL**, est destinée au dépôt et à la diffusion de documents scientifiques de niveau recherche, publiés ou non, émanant des établissements d'enseignement et de recherche français ou étrangers, des laboratoires publics ou privés.

Effect of an electric field on ferroelectric and piezoelectric properties of the brownmillerite $\text{Ca}_2\text{Al}_2\text{O}_5$

R. Arras,¹ C. Paillard,² and L. Bellaïche³

¹*CEMES, Université de Toulouse, CNRS, 29 rue Jeanne Marvig, F-31055, Toulouse, France**

²*Université Paris-Saclay, CentraleSupélec, CNRS,
Laboratoire SPMS, 91190 Gif-sur-Yvette, France*

³*Physics Department and Institute for Nanoscience and Engineering,
University of Arkansas, Fayetteville, Arkansas 72701, USA*

Brownmillerites $\text{A}_2\text{B}_2\text{O}_5$ are oxides possessing a crystallographic structure that is parent from the perovskite structure ABO_3 with an ordered sublattice of oxygen vacancies, forming a network of 1D chiral chains of oxygen tetrahedra carrying electric dipoles. The distribution of left- and right-handed chains enables the formation of different, polar or non-polar crystallographic phases with close internal energies. We have performed first-principles calculations on the non-magnetic $\text{Ca}_2\text{Al}_2\text{O}_5$ oxide, chosen as a case study, in order to study the effect of an external electric field, applied in the direction parallel to the chains, on the stability of four different crystallographic phases. We found that reversing the direction of the electric polarization in the *Ima2* phase necessitates going through different intermediate phases. However, we also showed that, even if the application of the electric field allows to change the relative stability of each phase, it cannot be sufficient to change one chain handedness at low temperature, owing to the high barrier energies, of the order of ~ 1 eV per chain of two tetrahedra, which has to be overpassed. Switching between different phases would thus require applying an electric field at high temperature or with the application of additional stress. Finally, we demonstrated that polar phases, such as *Ima2* or *Pmc2₁*, display negative longitudinal piezoelectric coefficients due to the lattice response to the applied electric field.

I. INTRODUCTION

Brownmillerite oxides of chemical formula $\text{A}_2\text{B}_2\text{O}_5$ (or, equivalently, $\text{ABO}_{2.5}$) possess a structure similar to the structure of perovskite oxides (of chemical formula ABO_3) in which oxygen vacancies are ordered and form 1D channels, all aligned along a specific crystallographic direction. These oxides have already shown a wide range of properties because of the numerous combinations of A and B cations which can be used to new compounds [1, 2] with different lattice distortions, oxidation states and magnetic ordering, providing a large range of functional properties. Hence, this family of oxides could help to enrich the list of multifunctional materials. Multiferroicity has, for example, been evidenced in materials such as $\text{SrFeO}_{2.5}$ [3] and studied theoretically in $\text{Ca}_2(\text{Fe,Al})\text{O}_5$ [4]. Brownmillerites are nowadays increasingly studied and could be as promising as their perovskite parents for future applications.

The particular tunabilities of brownmillerite properties is generally explained by the configurations of the chains of oxygen tetrahedra (T chains) formed because of the oxygen-vacancy channels. Similarly to the octahedra tilts observed in perovskite oxides, the oxygen tetrahedra can display tilts which make the associated chains to be chiral. Different control parameters and stimuli (chemical composition, temperature, strain, applied electric field) can be used to tune the atomic structure by changing the tetrahedra-tilts pattern [4, 5], the T-chain crystallographic orientations [6–8] or the oxygen content through

topotactic phase transitions ($\text{ABO}_{2.5}$ brownmillerites being an intermediate structure between ABO_3 perovskites and ABO_2 structures with infinite square lattices) [7, 9–13], all of this resulting in modifications of electronic, optical and magnetic properties. Topotactic transitions through brownmillerite structures is in particular promising for memristive devices and neuromorphism computing [7, 8, 13–15], as the anisotropic mobility of oxygen atoms is facilitated along the oxygen-vacancy channel, which moreover reduces the variability of the switching mechanisms [15].

If several research efforts have been dedicated to the study of topotactic transitions, the ordering of oxygen-tetrahedra tilts between different T chains remains an important characteristic of brownmillerites, as it is intimately linked to the possible emergence of a ferroelectric polarization in these oxides [3–5, 16]. Brownmillerites indeed display a non-conventional ferroelectricity, which comes from cation-oxygen displacements resulting from these oxygen-tetrahedra tilts. The collective tilts in each T chain result in left- or right-handed chiralities (noted “–” and “+” in the following) and are responsible of the emergence of electric dipoles along the [010] direction, the signs of which are defined by the chiral orientation of the T chains. The distribution of the orientations of the different chains will determine the value of the macroscopic electric polarization [16]. Finally, confirming the complexity of this system, Tian *et al.* [17] demonstrated that the ferroelectric state in the *Pmc2₁* ground state of $\text{Sr}_2\text{Co}_2\text{O}_5$ originates from a novel coupling between different phonon modes, which differs from those characteristic of the proper, improper [18], hybrid improper [19–22] or triggered [23, 24] type of ferroelectricity.

* remi.arras@cemes.fr

The chemical composition is the first important criterion to explain the stabilization of a particular (polar or non-polar) crystallographic phase. From a series of measurements on $\text{La}_{1-x}\text{A}_x\text{MnO}_{2.5}$ (with $\text{A} = \text{Ba}, \text{Sr}, \text{Ca}$), Parsons *et al.* [16] showed that the chain handedness ordering can be tuned by changing the chemical composition of A cation *via* two effects. Firstly, by changing the interlayer distances between two (001) T atomic layers. Secondly, by modifying the distortions on the T chains, which is a result of the change of Mn oxidation degrees in octahedral sites. Different structures can thus be generated as a function of the tilts patterns. The *Ima2* structure, which corresponds to the case with all T chains having the same handedness, can be stable when the net electric dipole is small. When electric dipole is too large, a centrosymmetric structure will form to compensate it: the structure will then possess an intralayer antiferroelectric ordering (*Pbcm*) if the separation distance between two adjacent T layers is large, while it will favor an interlayer antiferroelectric ordering otherwise, as such ordering does not involve a strong distortion of the oxygen octahedra [16, 25, 26]. In this latter case a *Pnma* structure will form, with all tetrahedra T chains in T and T' layers having chains with opposite chiralities. More generally, explanations of the structural ground states have been given through the use of several structural descriptors characterizing the distortions in terms of chemical bond-angles and lengths changes [5, 16]. For certain brownmillerites, or when the temperature is increased, the chain orientations can be disordered, leading to an *Imma* structure and (3+1)D *Imma*(00 γ)*s*00 superspace groups have even been often characterized to describe the formation of incommensurate orderings [27–29]. In addition to the choice of chemical composition, it has been found that the physical control of phases in brownmillerites is strongly dependent on the strain [5].

Applying an external electric field would be another way to modify the brownmillerite structure and properties. Experimentally, it has been shown that it could help to modify the T-chain crystallographic orientation [7] or to activate the oxygen conduction [7, 8, 15]. To our knowledge, no study has been reported on the effect of an electric field on the oxygen-tetrahedra tilts and of the T-chain handedness pattern, despite the fact that, as demonstrated in the case of perovskites [30], this would be important to understand the modification of ferroelectric properties, in view of integrating such materials in electronic devices.

In this paper, we show how the electric polarization can be reversed or tuned by an applied electric field in $\text{Ca}_2\text{Al}_2\text{O}_5$. We demonstrate that the electric field mostly induces an additional contribution to the polarization by displacing cations and anions in directions parallel/antiparallel to the electric field, while the tetrahedral-tilt patterns remain robust. We also show that the reversal of the spontaneous electric polarization is not homogeneous and requires to overcome high energy barriers. Finally, we discuss the lattice-strain response to the

electric field which is linked to a longitudinal negative piezoelectric coefficient.

II. DETAILS ON THE CALCULATION METHODS AND ON THE BROWNMILLERITE STRUCTURE

We performed first-principles calculations based on the density functional theory (DFT) [31, 32], using the VASP software [33, 34]. We employed the projector augmented wave method (PAW) [35] with a cutoff energy of 550 eV. The exchange-correlation functional was expressed within the generalized-gradient approximation parametrized by Perdew, Burke and Ernzerhof and revised for solids (GGA-PBESol) [36]. The first Brillouin zone was sampled using a Monkhorst-Pack grid [37] with dimensions $4 \times 6 \times 2$.

The external electric field is applied using the method proposed in Ref. [30]. The stability of the atomic structure is then governed by the energy F , which is, at a temperature of 0 K, equal to the Kohn-Sham internal energy U plus an additional electric-field (\mathcal{E}) dependent contribution, such that $F = U - \mathbf{P} \cdot \mathcal{E}$. The electric polarization \mathbf{P} has been calculated using the Born effective charges Z^* (calculated for the centrosymmetric *Imma* phase and given in Appendix A); this method is also convenient as it allows to perform a projection in a given volume [illustrated by the black dotted lines in Fig. 1(a)] to separate each T-chain contribution. For some polar bulk structures, we also calculated the total electric polarization using the Berry-phase method and found a fairly good agreement between the results obtained with both methods. To optimize the atomic structures, we calculated the total forces applied on each atom, which are now the sum of the standard Hellmann-Feynman forces plus a product between its Born effective charge Z^* and the electric field \mathcal{E} . To calculate the barrier energy to switch between two structural states, we used the climbing-image nudged elastic band method (CI-NEB) implemented within the VTST package [38].

The brownmillerite structure corresponds to a perovskite structure with oxygen vacancies aligned along the $[110]_p$ direction (we denote by "p" the directions and lattice parameters of a perovskite cell, while, when no precisions are given, the lattice parameters are those of the brownmillerite structure), which corresponds to the $[010]$ direction (denoted as the y axis in Fig. 1) in the brownmillerite structure [1, 16]. Along the $[001]$ (or equivalently $[001]_p$) direction, the structure is composed by an alternation of layers with B cations located either in octahedra (O) or in tetrahedra (T) atomic sites formed by the sublattice of oxygen atoms and separated by atomic planes with A cations. The successive (001) atomic layers thus have the chemical composition AO-BO₂-AO-BO; if we only consider the layers containing B cations, the structure corresponds to the sequence OTOT', with T and T' being two atomic layers with oxygen tetrahedra

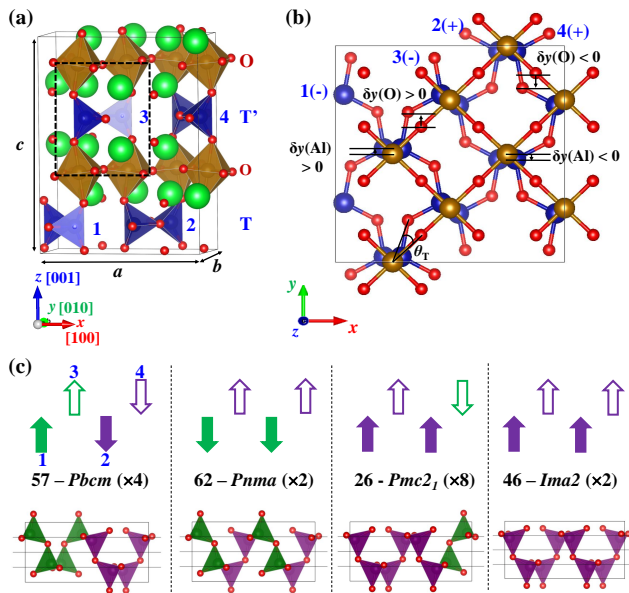


FIG. 1. (a) side and (b) bottom view of the brownmillerite structure with a $2\sqrt{2} \times \sqrt{2} \times 4$ supercell. The displayed structure corresponds to the most stable *Pbcm* space group, with two tetrahedra chains (in blue) having opposite chiralities in each (001) T atomic layers along the *c* axis. For the sake of clarity, we represented two cell periods along the *y* direction in Panel (b). (c) Atomic structures of the four more stable crystallographic structures generated from the different chiral-state patterns (12|34). The structures correspond to a projection onto the (001) plane and only the chains of tetrahedra are shown. The green and purple arrows give the orientation of the electric dipoles along the [010] direction; plain and empty arrows correspond to dipoles located in different (001) atomic layers. The black lines help to visualize the atomic displacements $\delta y(\text{Al})$ and $\delta y(\text{O})$ according to the centrosymmetric positions. The multiplicity of each structure is given between parentheses.

184 shifted one to each other along the $[1\bar{1}0]_p$ (or [100]) di-
 185 rection [see Fig. 1(a)]. Because of the oxygen-vacancies
 186 ordering, the oxygen tetrahedra in the T and T' layers
 187 form so-called *zweier* single chains [28] oriented along
 188 a $\langle 110 \rangle_p$ direction and associated with oxygen-vacancy
 189 channels. The studied structures are orthorhombic with
 190 lattice parameters $a \simeq 2\sqrt{2}a_p$, $b \simeq \sqrt{2}b_p$ and $c = 4c_p$,
 191 with *a*, *b* and *c* being respectively along the $[1\bar{1}0]_p$, $[110]_p$
 192 and $[001]_p$ directions. With these new basis vectors, the
 193 tetrahedra chains are oriented along the [010] direction,
 194 i.e. the *y* axis. The given supercell contains eight for-
 195 mula units (f.u.) of $\text{Ca}_2\text{Al}_2\text{O}_5$ and four T chains of two
 196 tetrahedra.

197 III. RESULTS

198 A. Properties of bulk $\text{Ca}_2\text{Al}_2\text{O}_5$ brownmillerite

199 We chose to focus our study on the $\text{Ca}_2\text{Al}_2\text{O}_5$ brown-
 200 millerite [29, 39, 40]. This oxide has not been exten-
 201 sively studied but it possesses the advantages to contain
 202 only one type of cation A and one type of cation B with
 203 both being non-magnetic. It is derived from the native
 204 $\text{Ca}_2(\text{Fe}_{1-x}\text{Al}_x)_2\text{O}_5$ brownmillerite, which has been found
 205 to naturally exist and which can be grown at ambient
 206 pressures for compositions *x* ranging from *x* = 0 to *x* =
 207 0.7 [41, 42]. Al-rich phases of $\text{Ca}_2(\text{Fe}_{1-x}\text{Al}_x)_2\text{O}_5$ gener-
 208 ally adopt a *Ima2* (or *I2mb*) space group [29, 40], while
 209 iron-rich phases (below *x* = 0.235) have been reported
 210 with a *Pnma* structure [28, 43]. Both for Al-rich or Fe-
 211 rich phases, a transition to an incommensurate struc-
 212 ture, with a superspace group (3+1)D *Imma*(00 γ)*s*00,
 213 has been evidenced at high temperature [28, 29]. The
 214 experimental synthesis of $\text{Ca}_2\text{Al}_2\text{O}_5$ (that is for *x* = 1)
 215 requires high pressure and high temperature, and it is
 216 then possible to quench the material at room tempera-
 217 ture (see Ref. [29] and references therein) in order that
 218 the system stays in the brownmillerite structure.

219 *a. Stability of the different crystallographic phases:*
 220 $\text{Ca}_2\text{Al}_2\text{O}_5$ can exist under different crystallographic
 221 phases, which differ one from another by their pattern of
 222 chain handedness. With our considered supercells, these
 223 pattern of chain handedness will be noted (12|34), where
 224 1-4 are the chain numbers given in Fig. 1. The right- or
 225 left-handed enantiomorphic chains will be noted + and
 226 -, respectively, and 0 will correspond to an average state,
 227 when the tetrahedra display no rotation.

228 The aristotype *Imma* space group (No 74) corresponds
 229 to the brownmillerite structure (12|34) = (00|00) with
 230 no tetrahedra tilts. Using the supercell described in the
 231 previous section, it is then possible to generate four het-
 232 totypic structures, as shown in Fig. 1(c). Table I summa-
 233 rizes the main properties of each of these structures.

234 The *Ima2* structure (No 46) is non-centrosymmetric
 235 and possesses only T chains with one specific handedness
 236 ("-" or "+") defined from the tetrahedra-tilts direction.
 237 This structure thus displays a spontaneous electric po-
 238 larization that we calculated to be $P_{\text{tot}}^0 = 3.8 \mu\text{C cm}^{-2}$
 239 by using Born effective charges; a slightly lower value of
 240 $3.6 \mu\text{C cm}^{-2}$ was obtained using the Berry-phase method.
 241 By changing the intralayer relative chain direction, it is
 242 possible to switch from this *Ima2* structure (+ + | + +)
 243 to the *Pbcm* non-polar structure (+ - | + -) (No 57),
 244 which corresponds to our calculated ground state struc-
 245 ture and which is more stable than the *Ima2* structure
 246 by 0.08 meV/f.u. according to our simulations. Still
 247 from the *Ima2* polar structure, it is also possible to
 248 generate the less stable centrosymmetric *Pnma* struc-
 249 ture (- - | + +) (No 62), by modifying the interlayer
 250 ordering. Finally, the intermediate *Pmc2*₁ structure
 251 (+ - | + +) (No 26), associated with an electric polariza-
 252 tion of $1.9 \mu\text{C cm}^{-2}$ ($1.2 \mu\text{C cm}^{-2}$ with the Berry-phase

TABLE I. Lattice parameters (a, b, c), averaged tetrahedra tilts $\langle|\theta_T|\rangle$, local and total electric polarizations P_α and P_{tot}^0 , and internal energy U per formula unit of $\text{Ca}_2\text{Al}_2\text{O}_5$. The zero of energy is chosen for the ground state, $Pbcm$.

Space group		Chiral states	a	b	c	$\langle \theta_T \rangle$	$\langle\Delta y_T\rangle$	P_α				P_{tot}^0	U
			(Å)	(Å)	(Å)	(°)	Å	$\mu\text{C cm}^{-2}$				$\mu\text{C cm}^{-2}$	meV/f.u.
Number	Name							1	2	3	4		
74	<i>Imma</i>	(00 00)	10.8223	5.3603	14.0670	0.00	0.00	0.00	0.00	0.00	0.00	0.00	468.55
57	<i>Pbcm</i>	(+ - + -)	10.8093	5.2306	14.3532	25.73	0.00	0.86	-0.86	0.86	-0.86	0.00	0.00
62	<i>Pnma</i>	(- - + +)	10.8123	5.2274	14.3593	25.63	0.00	1.02	1.02	-1.02	-1.02	0.00	2.92
26	<i>Pmc2₁</i>	(+ - + +)	10.8115	5.2288	14.3539	25.67	0.23	0.99	0.99	0.82	-0.90	1.90	0.89
46	<i>Ima2</i>	(+ + + +)	10.8144	5.2280	14.3489	25.61	0.46	0.96	0.96	0.96	0.96	3.85	0.08
46	<i>Ima2</i> ^a	(+ + + +)	10.8008	5.2281	14.4686								
74.2	<i>Imma(00γ)s00</i> ^b		10.8392	5.2699	14.6984								

^a Experimental, measured at room temperature [40].

^b Experimental, measured at $T = 1090$ K [29].

method), is obtained by changing the tilts direction in only one chain from the three previous structures (*Ima2*, *Pnma* and *Pbcm*). To summarize, with a brownmillerite supercell with four T chains, it is possible to generate four non-equivalent structures. It is important to note that different tilts patterns can correspond to the same structure, the four structures *Ima2*, *Pmc2₁*, *Pbcm* and *Pnma* hence having a multiplicity of 2, 8, 4 and 2, respectively.

From Table I, we can see that the calculated lattice parameters are in fairly good agreement with reported experimental parameters, with a calculated pseudocubic lattice parameter for the *Ima2* phase only 0.23% lower than the experimental value [40]. From our calculations, we can also see that the variation of lattice parameters between the different crystallographic phases is quite small for the four more stable phases (-0.01% in average between the *Pbcm* and *Ima2* phases), while it is more important if we consider the *Imma* phase (-0.19% with the *Pbcm* phase). The larger lattice distortion separating the *Imma* phase from the four other structures is in agreement with the calculated high internal energy. The in-plane distance separating two T chains only decreases by 0.26 pm when changing from the *Ima2* to the *Pbcm* phase, while the out-of-plane distance increases by 0.52 pm when switching from the *Ima2* to the *Pnma* phase. For the four structures, *Ima2*, *Pmc2₁*, *Pnma* and *Pbcm*, the averaged absolute value of the tetrahedra-tilt angles $\langle|\theta_T|\rangle$ does not strongly vary and remains in the range of 25.61-25.73°. Depending on the handedness of the T chain, the Al cations and anions are all displaced in the same direction along the y axis. For example, in the case of the *Ima2* structure, we found that the Al atoms are, in average, displaced from their centrosymmetric positions by $\delta y(\text{Al}) = -18.4$ pm, and the oxygen atoms by $\delta y(\text{O}) = -64.5$ pm, so that the cation-oxygen buckling is of $\Delta y_T(\text{Ima2}) = \delta y(\text{Al}) - \delta y(\text{O}) = 46.1$ pm. The spontaneous electric polarization is really dependent on the distortions located in the T and T' layers; if we calculate a similar averaged oxygen-cation buck-

ling in the O layer, we indeed find a much lower buckling of $\langle\Delta y_O(\text{Ima2})\rangle \simeq 0.7$ pm. In the case of the *Pbcm* phase, we calculated larger atomic displacements $\delta y(\text{O}) = \pm 72.2$ pm and $\delta y(\text{Al}) = \pm 26.0$ pm (the sign depends on the considered chain and its handedness), which however still corresponds to a similar cation-oxygen buckling, in a given chain, of $\Delta y_T(\text{Pbcm}) = \pm 46.2$ pm. The buckling values $\langle\Delta y_T\rangle$ averaged on the four T chains follow the same trends as the electric polarization, which is proportional to the number of + and - chains.

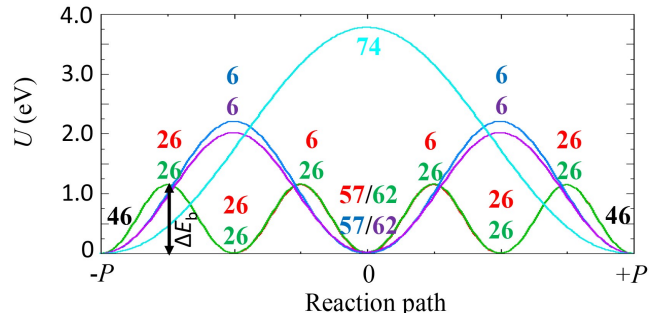


FIG. 2. Barrier energies calculated to switch between two *Imma* phases with electric polarization equal to $-P$ and to $+P$. Several reaction paths, involving different intermediate crystallographic phases, are shown: by switching the chains one by one [46 \rightarrow 26 \rightarrow 57 \rightarrow 26 \rightarrow 46 (red) and 46 \rightarrow 26 \rightarrow 62 \rightarrow 26 \rightarrow 46 (green)], two by two [46 \rightarrow 57 \rightarrow 46 (dark blue) and 46 \rightarrow 62 \rightarrow 46 (purple)] and all at the same time [46 \rightarrow 46 (cyan)]. The numbers given above the curves correspond to the space groups adopted during the reaction path at each maximum and minimum. Because of their relatively close energies, the red and green curves are almost superimposed. The barrier energies are calculated using the supercell presented in Fig. 1a, in which a T chain period is formed by two AlO_4 tetrahedra. The atomic structures associated to the red curve can be seen in Fig. 8.

^b *Energy barrier to switch between the different phases:* The NEB method was used to calculate the energy barrier ΔE_b , which has to be overcome to reverse the

306 electric polarization in the case where the *Ima2* phase is
 307 stabilized. $\Delta E_b(\alpha \rightarrow \beta)$ is defined as the energy dif-
 308 ference between the maximum of the energy calculated
 309 along a reaction path between two states α and β and
 310 the energy of the initial state α .

311 A homogeneous switching, corresponding to a direct
 312 $46 \rightarrow 46$ transition, would require to rotate simultane-
 313 ously all T chains and the maximum of the energy bar-
 314 rier would be reached when all tetrahedra tilts $\theta_T = 0^\circ$,
 315 *i.e.*, when the structure takes the *Imma* space group. In
 316 that case, as displayed in Fig. 2, the total energy bar-
 317 rier for the whole heterostructure is thus expected to be
 318 $\Delta E_b(46 \rightarrow 46) = 3.78$ eV, or 0.95 eV per chain of two
 319 tetrahedra. Such energy barrier is high if we compare it
 320 to common ferroelectric materials for which the energy
 321 required to switch the electric polarization is in the order
 322 of tens of meV [44]. On the other hand, our calculated
 323 value is closer to the energy barriers reported for geo-
 324 metric ferroelectrics [21], in which the ferroelectricity is
 325 driven by rotations and it is approximately three times
 326 higher than the value calculated for the Brownmillerite
 327 $\text{Sr}_2\text{Fe}_2\text{O}_5$ [3]. The high energy necessary to change the
 328 T-chain handedness may be easily understood from geo-
 329 metry considerations, taking into account that a T chain
 330 is formed by a succession of oxygen tetrahedra turning al-
 331 ternatively in clockwise and anticlockwise directions and
 332 changing the chain handedness would require to reverse
 333 simultaneously the angles of all tetrahedra. It is impor-
 334 tant to note that these calculated energy barriers are of
 335 the same order of magnitude than those calculated for
 336 the migration of oxygen atoms between different atomic
 337 sites [15, 45].

338 Up-to-now, we considered that the polarization rever-
 339 sal was performed by homogeneously switching all chains
 340 at the same time. It is however reasonable to assume that
 341 the polarization switching would rather occur by chang-
 342 ing the handedness of the T-chains one after another,
 343 eventually through the motions of domain walls [44, 46].
 344 Locally, such process could allow to generate different in-
 345 termediate states corresponding to phases like those dis-
 346 cussed before. For this reason, we also calculated the
 347 energy barriers to transit between the different phases
 348 by switching only one or two chains at the same time.
 349 Because of the distortions induced in the structure in the
 350 near environment of the chain with rotating tetrahedra
 351 and the structural connections with other chains, rotat-
 352 ing separately the chains increases slightly the chain bar-
 353 rier energy to 1.10 eV and 1.15 eV per chain of two tetra-
 354 hedra, if two or one chains are rotating at the same time,
 355 respectively (these energies are always given according
 356 to the energy of the *Ima2* phase). We can indeed see
 357 in Fig. 3(a) that rotating oxygen tetrahedra in a specific
 358 chain (*e.g.*, chain 1) induces also a very small variation
 359 of tilt angles in the chain belonging to the same (001)
 360 atomic layer (*i.e.*, chain 2). This may also explain why
 361 the energy barriers $\Delta E_b(62 \rightarrow 46)$ is lower by 21 meV
 362 than the barrier $\Delta E_b(57 \rightarrow 46)$. The structural cou-
 363 pling between the different T chains and the induced

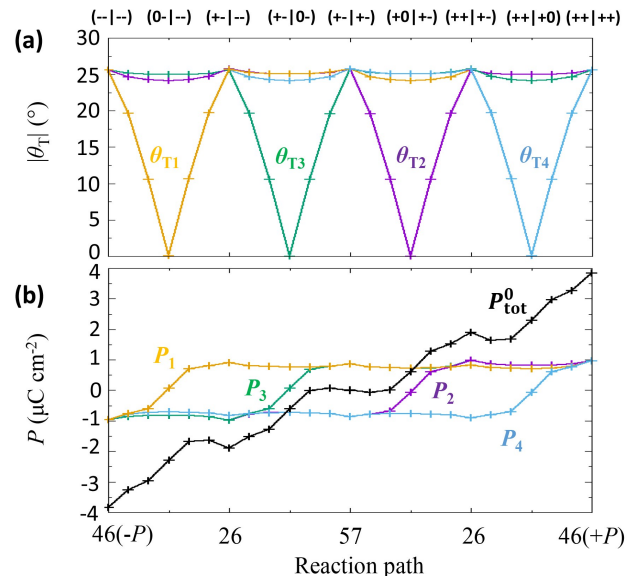


FIG. 3. Variations of (a) tilt angles $|\theta_T|$ and (b) local elec-
 tric polarization P_α associated to the T chains (12|34) along
 the reaction path $46 \rightarrow 26 \rightarrow 57 \rightarrow 26 \rightarrow 46$ (red curve in
 Fig. 2). The local electric polarization P_α are calculated by
 summing the contributions of atoms located in a volume cen-
 tered around a given T chains and as defined by the black
 dotted lines of Fig. 1(a).

364 structural distortions are however relatively low and, in
 365 a first approximation, we can consider that each chain
 366 behaves almost independently: as discussed before and
 367 displayed in Fig. 3(b), each chain-state reversal increases
 368 approximately the total electric polarization by, in av-
 369 erage, $P_\alpha \simeq 0.94 \mu\text{C cm}^{-2}$. This result is in agreement
 370 with the relation $P_{\text{tot}}^0(\text{Ima2}) = 2P_{\text{tot}}^0(\text{Pmc2}_1)$ linking the
 371 polarizations calculated for the two polar states and with
 372 the individual chain contributions P_α to the total polar-
 373 ization displayed in Tab. I, which only vary by $\pm 8.5\%$ in
 374 magnitude, depending on the states of the surrounding
 375 chains.

376 B. Effect of an electric field parallel to the chains

377 Since the spontaneous electric polarization in the
 378 brownmillerite structure depends on the tilt pattern, we
 379 tried to verify if it is possible to change the rotation
 380 direction of the T chains, and therefore to switch be-
 381 tween different crystallographic phases by applying an
 382 electric field. Our calculations were performed by adding
 383 the effect of an electric field ranging from -4×10^9 to
 384 $4 \times 10^9 \text{ V m}^{-1}$ and oriented along the $b[010]$ axis, *i.e.*,
 385 the direction of the electric dipoles in the four phases
 386 *Pbcm*, *Pnma*, *Ima2* and *Pmc2}_1*. Because the electric
 387 field is applied in the direction (anti)parallel to the elec-
 388 tric polarization of the polar phases, their space group
 389 will remain the same; on the contrary, the electric field

390 will break the inversion symmetry of non-polar phases
 391 and the $Pnma$ structure will turn in a structure with
 392 $Pmc2_1$ space group, while the $Pbcm$ structure will trans-
 393 form into $Pma2$ (No 28). For the sake of simplicity, we
 394 will continue to call the structure using their space group
 395 at zero field.

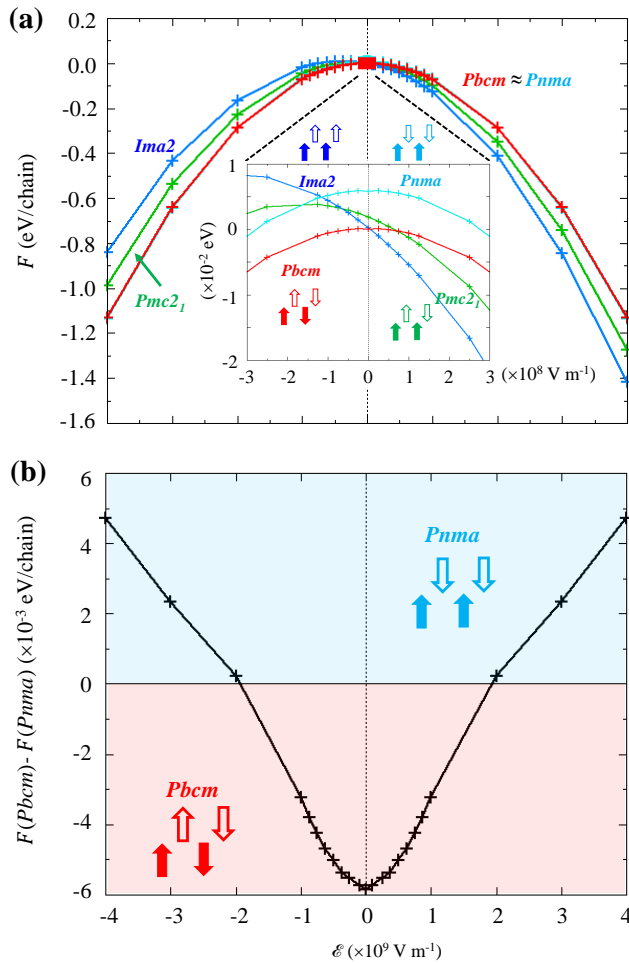


FIG. 4. (a) Free energy F as a function of the electric field \mathcal{E} applied to the four studied crystallographic phases of $\text{Ca}_2\text{Al}_2\text{O}_5$. (b) Difference of free energies calculated between the $Pbcm$ and $Pnma$ phases. As in Fig. 1c, the arrows indicate the configuration of electric dipoles in each crystallographic phase.

396 *a. Thermodynamic stability:* In Fig. 4(a), we display
 397 the evolution of the free energy F calculated for the different
 398 crystallographic phases and as a function of the applied electric
 399 field \mathcal{E} . First of all, we can notice that the variation of F
 400 is symmetrical for the non-polar phases $Pbcm$ and $Pnma$, while
 401 it is not the case for the polar phases $Ima2$ and $Pmc2_1$, for
 402 which the value of the free energy depends on the direction of
 403 the electric field, which can be parallel (positive values) or
 404 antiparallel (negative) to the spontaneous polarization P_{tot}^0
 405 calculated at zero field.

406 As discussed in the previous section, when no electric

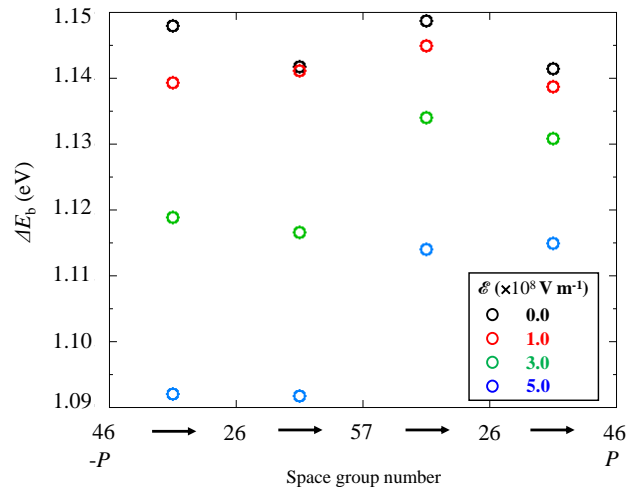


FIG. 5. Energy barriers to switch between the different indicated crystallographic phases and to fully reverse the electric polarization of the $Ima2$ phase, with/without an applied electric field of 10^8 to $5 \times 10^8 \text{ V m}^{-1}$.

408 field is applied, the non-polar $Pbcm$ phase corresponds
 409 to the ground state, but it displays only a rather small
 410 energy difference, of 0.08 meV/f.u. , with the second most
 411 stable phase, which is the polar $Ima2$ structure. In the
 412 presence of a parallel external electric field with a mag-
 413 nitude greater than $\mathcal{E} = +4.6 \times 10^6 \text{ V m}^{-1}$, this polar
 414 phase becomes more stable, and the intermediate (and
 415 also polar) $Pmc2_1$ phase the second most stable from
 416 $\mathcal{E} = +7.2 \times 10^7 \text{ V m}^{-1}$. On the contrary, it can be seen
 417 that, if the electric field is applied antiparallel, the two
 418 non-polar phases not only remain the more stable states,
 419 but their energy difference with respect to the energies
 420 of the polar phases increases with the magnitude of \mathcal{E} .

421 Comparing the two non-polar phases, we can see in
 422 Fig. 4(a) that the two curves representing the variation of
 423 their free energy are almost superimposed, which shows
 424 that their energy difference remains low – in comparison
 425 with the energy difference with other phases, even at high
 426 electric-field values. In Fig. 4(b), we can indeed see that
 427 the energy difference between these two non-polar phases
 428 is at most 5.8 meV/chain of two tetrahedra. From this
 429 figure, we can also see that the energy difference between
 430 these two phases as a function of \mathcal{E} is not really constant
 431 and it appears that the $Pnma$ structure becomes the
 432 most stable structure above $|\mathcal{E}| = 1.9 \times 10^9 \text{ V m}^{-1}$.

433 If we come back to the energy path $46(-P) \rightarrow 26 \rightarrow$
 434 $57 \rightarrow 26 \rightarrow 46(+P)$ calculated in Fig. 2 (red curve), we
 435 can wonder how the calculated energy barriers ΔE_b vary
 436 when an electric field of $\mathcal{E} = +10^8 \text{ V m}^{-1}$ (antiparallel
 437 to the initial polarization $-P$) is applied. As shown in
 438 Fig. 5, we found that these barriers will be reduced by
 439 at most $\sim 9 \text{ meV}$ when switching between the $46-Ima2$
 440 and the $26-Pmc2_1$ phases, and by $\sim 1 \text{ meV}$ between the
 441 $26-Pmc2_1$ and $57-Pbcm$ phases, which corresponds to a
 442 maximum reduction of only 0.75% if compared to the

443 energy barrier without any electric field. Because higher
 444 electric fields can be experimentally applied in thin films,
 445 we calculated the barrier energies for higher magnitudes
 446 of \mathcal{E} : The energy barriers to switch the electric dipoles on
 447 one T chain become more homogeneous as we increase \mathcal{E} ,
 448 but they remain very high, of around 1.092 eV when the
 449 electric field is of $+5 \times 10^8 \text{ V m}^{-1}$ and that the global elec-
 450 tric polarization is still antiparallel to it, and 1.114 eV,
 451 when the electric field and the electric polarization are
 452 parallel.

453 According to our calculations, it appears that, even
 454 by applying a large electric field, it should be difficult
 455 to switch between different crystallographic phases, at
 456 least at a temperature of 0 K. It is indeed interesting
 457 that Kang, *et al.* [3], demonstrated the possibility to re-
 458 verse the electric polarization at room temperature in
 459 a thin film of $\text{Sr}_2\text{Fe}_2\text{O}_5$ in its *Ima2* ferroelectric phase;
 460 they estimated that the electric coercive field was about
 461 $1.5 \times 10^8 \text{ V m}^{-1}$. The ability to reverse the electric po-
 462 larization with such an electric field might highlight the
 463 importance of domain-wall motion in the polarization-
 464 switching mechanism of brownmillerites.

465 Finally, we can also address the idea that, if the sys-
 466 tem is initially in a non-polar state, it could be possible
 467 to stabilize the polar phase *Ima2* by heating the sample
 468 and by applying the electric field at a sufficiently high
 469 temperature; if we then slowly cool down the system in
 470 order to keep it in equilibrium in the polar *Ima2* phase,
 471 we can expect to preserve this state down to room tem-
 472 perature. This state should then be locked, even after
 473 removing the electric field.

474 *b. Evolution of the electric polarization:* From the
 475 NEB calculations described previously, we saw that the
 476 energy cost to reverse the T-chain handednesses, which
 477 are linked to the spontaneous electric polarization P_{tot}^0 at
 478 zero electric field, is very high. The electric field applied
 479 in our calculations will nonetheless modify the atomic
 480 structure and induce an additional contribution to the
 481 electric polarization. As displayed in Figs. 6(a,b), the
 482 total electric polarization is increasing quasi-linearly, as
 483 a function of the electric field, between $\mathcal{E} = -10^9$ and
 484 $+10^9 \text{ V m}^{-1}$, with a slope of $11.24 \times 10^{-11} \text{ F m}^{-1}$ and
 485 $11.04 \times 10^{-11} \text{ F m}^{-1}$, for the polar *Ima2* and non-polar
 486 *Pbcm* phase, respectively. We calculated similar dielec-
 487 tric response (not shown) for the two other phases, with
 488 $\frac{dP_{\text{tot}}}{d\mathcal{E}} = 11.39 \times 10^{-11} \text{ F m}^{-1}$ for the *Pnma* phase and
 489 $11.20 \times 10^{-11} \text{ F m}^{-1}$ for the *Pmc2*₁ one. An additional
 490 cubic contribution ranging from $-0.065 \times 10^{-10} \text{ F m V}^{-2}$
 491 (*Ima2*) to $-0.090 \times 10^{-10} \text{ F m V}^{-2}$ (*Pnma*) starts also
 492 to be visible for the highest values of electric field, that
 493 is above 10^9 V m^{-1} . The dielectric response is thus not
 494 expected to vary significantly depending on the stabi-
 495 lized crystallographic phase, even if we calculated slightly
 496 larger coefficients for the polar phases. On the contrary
 497 to the polar phases, such as the *Pbcm* structure, for po-
 498 lar phases like *Ima2*, we can note a small asymmetry
 499 of the curve, which is due to the non-null initial po-
 500 larization P_{tot}^0 , which is never reversed (each T chain

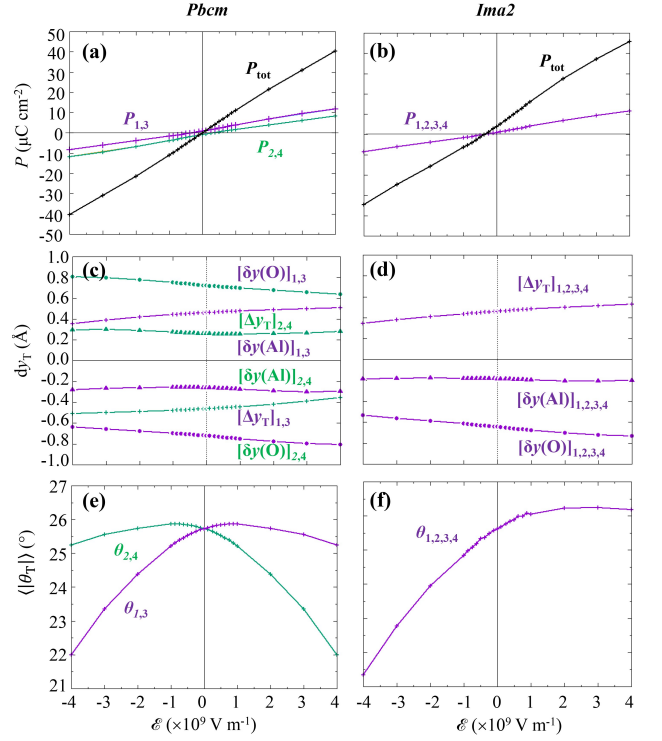


FIG. 6. Total and local electric polarization, P_{tot} and P_{α} respectively, as a function of the applied electric field \mathcal{E} and calculated for the (a) *Pbcm* and (b) *Ima2* phases. (c,d) Atomic displacements and (e,f) Tetrahedra tilt angles $|\theta_{\text{T}}|$ also calculated as a function of \mathcal{E} .

501 preserves its initial handedness) due to the large energy
 502 barriers, as explained in the previous sections. The to-
 503 tal electric polarization under the application of an elec-
 504 tric field could indeed be expressed as a sum of the ini-
 505 tial polarization P_{tot}^0 and an induced polarization $P_{\text{tot}}^{\text{ind}}$:
 506 $P_{\text{tot}}(\mathcal{E}) = P_{\text{tot}}^0 + P_{\text{tot}}^{\text{ind}}(\mathcal{E})$. The initial and spontaneous
 507 polarization P_{tot}^0 , which is associated to the tetrahedra
 508 tilts, should stay quasi-constant. The induced polariza-
 509 tion is associated to the linear ionic response to the elec-
 510 tric field $P_{\text{tot}}^{\text{ind}}(\mathcal{E}) = \chi_i \varepsilon_0 \mathcal{E}$, with χ_i the ionic contribu-
 511 tion to the electric susceptibility and ε_0 the vacuum permi-
 512 tivity. The free energy can then be re-written as:

$$F(\mathcal{E}) = F^0 - P_{\text{tot}}^0 \mathcal{E} - \chi_i \varepsilon_0 \mathcal{E}^2 \quad (1)$$

513 For the *Ima2* structure, we also performed a calcula-
 514 tion using the density perturbation functional theory
 515 (DFPT) [47, 48] to calculate the susceptibility and we
 516 found that $\chi \varepsilon_0 = 12.8 \times 10^{-11} \text{ F m}^{-1}$ (χ being the to-
 517 tal susceptibility), which is in good agreement with our
 518 previous estimation.

519 While P_{tot}^0 can be parallel or antiparallel to the ap-
 520 plied electric field, $P_{\text{tot}}^{\text{ind}}(\mathcal{E})$ will always be parallel to it.
 521 In consequence, if P_{tot}^0 is parallel to the electric field, we
 522 expect that F will decrease as \mathcal{E} increases, and the free
 523 energy of the polar phases will always be lower than the
 524 free energy of the non-polar phases, the energy difference

525 between the different phases being equal to the differ-
 526 ence between their spontaneous polarization, multiplied
 527 by the magnitude of the electric field. If the sponta-
 528 neous polarization is antiparallel to the electric field, the
 529 free energy will first increase until it reaches a maximum
 530 at $\mathcal{E} = -\frac{P_{\text{tot}}^0}{\chi_i \epsilon_0}$, as shown in the inset of Fig. 4a; at high
 531 electric-field values, the non-polar phases will be the most
 532 stable.

533 According to the discussion above, we succeeded to
 534 understand why the polar or non-polar phases could be
 535 more stable according to the direction of the applied elec-
 536 tric field. From the Eq. 1, if we consider that χ_i does not
 537 strongly vary for the different crystallographic phases,
 538 we should conclude that the difference of free energy be-
 539 tween the different phases should vary linearly or remain
 540 constant if the two phases have initially the same electric
 541 polarization, which is not the case according to Fig. 4.
 542 Of course, we already saw that, at high electric field, the
 543 variation of the total electric polarization is not fully lin-
 544 ear anymore. In order to have a better insight in the
 545 mechanisms that govern the change of electric polariza-
 546 tion, we can decompose the total electric polarization in
 547 chain contributions P_α , as already done in Fig. 3(b). It
 548 is then possible to see in Figs. 6(a,b) that each P_α fol-
 549 lows the same trend than P_{tot} . To improve the analy-
 550 sis, we also chose to show in Figs. 6(c,d) the atomic dis-
 551 placements and the corresponding cation-anion bucklings
 552 Δy_{T} , and in Figs. 6(e,f) the variation of the tetrahedra-
 553 tilt angles $|\theta_{\text{T}}|$ as a function of \mathcal{E} .

554 Let us first consider the *Ima2* structure for simplic-
 555 ity. We can see that the cation-anion buckling along the
 556 [001] direction, $\langle \Delta y_{\text{T}} \rangle$, decreases by approximately 12 pm
 557 for each chain, when the electric field is antiparallel to
 558 the initial electric polarization and decreases from 0 to
 559 $-4 \times 10^9 \text{ V m}^{-1}$. We observe on the contrary a smaller
 560 increase by 7 pm, when the electric field is increased to
 561 $+4 \times 10^9 \text{ V m}^{-1}$. This variation of buckling is mostly
 562 governed by the displacement of oxygen atoms. Con-
 563 cerning the tetrahedra-tilt angles, again we can observe
 564 a stronger variation when the electric field is applied an-
 565 tiparallel to the initial electric polarization than when it
 566 is parallel, with a maximum decrease/increase of $5^\circ/0.6^\circ$
 567 in the considered electric-field range. The quasi-linear
 568 variation of the local and total polarizations P_α and P_{tot}
 569 as a function of the electric field can thus be mostly as-
 570 cribed to the linear response to the electric field, which
 571 results in a translation of cations and anions. The non-
 572 linear component can partly be attributed to the small
 573 variations of tilt angles θ_{T} , which appears to be mostly
 574 quadratic. These variations of tilt angles as a function
 575 of \mathcal{E} show that the spontaneous polarization arising from
 576 the tetrahedra tilts and that we first considered as con-
 577 stant, will display short variations, which may partly ex-
 578 plain the non-linear variation of P_{tot} at high electric field
 579 and why the difference of free energy between the differ-
 580 ent phases is also not linear. It is also important to keep
 581 in mind that $\langle \Delta y_{\text{T}} \rangle$ and $\langle |\theta_{\text{T}}| \rangle$ are quantities which are
 582 calculated from the Al-O atoms present in the T layers

583 only, while the local electric polarization P_α are calcu-
 584 lated in a volume including also surrounding atoms in
 585 consideration. These other sublattices will also undergo
 586 some distortions as it is already known to happen in per-
 587 ovskites.

588 Contrary to the *Ima2* phase, for which all the T chains
 589 are equivalent, the *Pbcm* phase displays two sets of chains
 590 [Fig. 6(a)], one with the local spontaneous polarization
 591 P_α^0 parallel and the other one antiparallel to the electric
 592 field, whatever its direction is. As it was noticed before,
 593 the behavior of each chain can be considered, at first,
 594 as independent. Their local polarizations present simi-
 595 lar slopes than the chains in the *Ima2* phase. We also
 596 observe the same trends for cation-anion bucklings and
 597 tetrahedra tilts, with mirror variations for the two sets
 598 of chains, due to the direction of their chain spontaneous
 599 polarization with respect to the electric field. If we an-
 600 alyze in more details the variations of P_α in the *Pbcm*
 601 phase, we can see that the slopes displayed by the two
 602 sets of chain is not exactly equal. We calculated that
 603 the polarization difference between two chains with op-
 604 posite handedness, $P_1 - P_2$ for example, increases from
 605 $1.7 \mu\text{C cm}^{-2}$ to $3.4 \mu\text{C cm}^{-2}$, when the electric field is
 606 increased between 0 and $4 \times 10^9 \text{ V m}^{-1}$. It is certainly
 607 partly due to the asymmetric variation of the tilt angles
 608 $\langle |\theta_{\text{T}}| \rangle$.

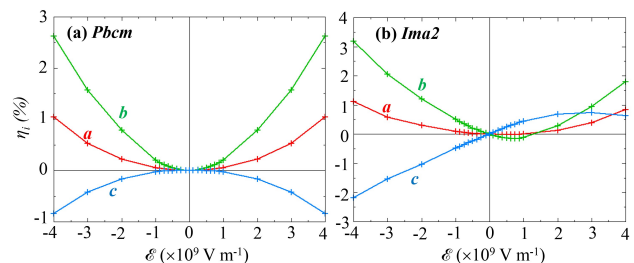


FIG. 7. Lattice strain η_i as a function of the applied electric field \mathcal{E} .

609 *c. Lattice strain:* Let us finally investigate the effect
 610 of applying an electric field on the lattice parameters, as
 611 shown in Fig. 7. We will characterize the variations of
 612 lattice parameters thanks to first-order and second-order
 613 coefficients, d_i and M_i respectively, obtained by fitting
 614 the lattice strain η as a function of \mathcal{E} in a range between
 615 -10^9 and $+10^9 \text{ V m}^{-1}$. These coefficients are reported in
 616 Table II. They may roughly correspond to converse piezo-
 617 electric and electrostrictive coefficients, but are mostly
 618 indicative as a precise calculation would require to use
 619 more accurate methods [49], which is beyond the scope
 620 of this paper. We define the lattice strain coefficients
 621 $\eta_i = (j - j_0)/j_0$, with $i = x, y, z$, $j = a, b, c$ and j_0 being
 622 the lattice parameter at zero electric field.

623 For the non-polar phases, such as the *Pbcm* structure
 624 [Fig. 7a], we fitted $\eta_i(\mathcal{E}) = M_i \mathcal{E}^2$ and we calculated a
 625 quasi-quadratic elongation of the in-plane lattice param-
 626 eters, which is approximately four times bigger for the *b*
 627 lattice parameter than for *a* – recalling that the *y*-axis

TABLE II. Piezoelectric and electrostrictive coefficients d_i and M_i calculated by fitting the variation of strain η_i as a function of an electric field \mathcal{E} applied along the [010] direction and with a magnitude varying between -10^9 and $+10^9$ V m $^{-1}$. Because the electric polarization and applied electric fields are along y , $d_x = d_{21}$, $d_y = d_{22}$ and $d_z = d_{23}$, in Voigt notations [50].

Space group	M_x	M_y	M_z	d_x	d_y	d_z
	$(\times 10^{-2} \text{ \AA}^2 \text{ V}^{-2})$			(pm V^{-1})		
<i>Pbcm</i>	5.00	20.28	-2.17	-	-	-
<i>Pnma</i>	5.84	22.72	-4.82	-	-	-
<i>Pmc2₁</i>	4.45	20.76	-3.10	-0.29	-1.68	2.41
<i>Ima2</i>	4.04	18.26	-1.47	-0.43	-3.30	4.71

is the direction of the electric field. The calculated large increase of the b lattice parameter is consistent with the increase of the electric polarization P_{tot} induced by the applied electric field. The elongation of in-plane lattice parameters is accompanied by a contraction of the out-of-plane lattice parameter c . The calculated coefficients thus reflect the anisotropic electrostrictive behavior (see Table II). In the previous subsection, we saw that the induced change of electric polarization could help to understand the (de)stabilization of polar phases over non-polar phases. Concerning the relative stability of the two non-polar phases *Pbcm* and *Pnma*, we also saw that their free energies remain very close, but that, from an electric field value of $\mathcal{E} = \pm 1.9 \times 10^9$ V m $^{-1}$, the *Pnma* phase becomes more stable than the *Pbcm* one. The calculated changes of lattice parameters could also explain this change of relative stability. Indeed, the *Pnma* phase could become more stable than the *Pbcm* structure because, when $|\mathcal{E}|$ increases, the decrease of c induces a consecutive increase of the interlayer chain interaction (which imposes an antiferroelectric ordering [16, 25, 26]), while the increase of the in-plane lattice parameter a , on the contrary, decreases the intralayer chain interaction.

When polar phases are stabilized [see Fig. 7b for the *Ima2* structure], on the contrary to the *Pbcm* structure, the electric field will have a different effect depending if it is applied parallel (positive values) or antiparallel (negative) to the electric polarization at zero field P_{tot}^0 . When the direction is antiparallel, the variation of lattice parameters follows the same trend than for the *Pbcm* phase, while, when it is parallel, we observe an increase of the out-of-plane lattice parameter c and a decrease of b , as the magnitude of \mathcal{E} increases up to 1.2×10^9 V m $^{-1}$. From Fig. 7b, it is also possible to see that the variation of the c parameter as a function of \mathcal{E} , when \mathcal{E} is low, is more linear than for the *Pbcm* phase. Because *Ima2* is non-centrosymmetric, the piezoelectric coefficients are expected to be non-zero. For this phase, we thus fitted the lattice-parameter curves by $\eta_i(\mathcal{E}) = d_i\mathcal{E} + M_i\mathcal{E}^2$. We found that along y and z , the piezoelectric and electrostrictive coefficients display opposite signs and relatively large values, which suggests that they govern the

strain variation at low electric fields.

Piezoelectric materials with negative longitudinal coefficients are relatively rare but have been reported in wurtzite BN [51], orthorhombic hafnia HfO $_2$ [52], ABC hexagonal ferroelectrics [53] or also in layered ferroelectrics like CuInP $_2$ S $_6$ [54]. The piezoelectric coefficient can be decomposed into the sum of two terms, the clamped-ion term, which is the component calculated for the equilibrium structure, i.e. at zero strain, and the internal-strain term [53, 55]. Negative piezoelectric coefficients have been found when the clamped-ion term is negative and dominates over the second term [53, 54], generally because this last one is small due to low Born effective charges or to small responses associated to the atomic positions, which can be the case in low-dimensional crystals [54]. On the contrary, in HfO $_2$, the lattice-mediated response has been found to dominate and to be at the origin of the negative coefficient. For Ca $_2$ Al $_2$ O $_5$, we calculated that the longitudinal coefficient coming from the ionic response d_y is negative. This ionic term depends on the calculated Born effective charges, given in Appendix A, which are not particularly small, with diagonal terms close to $\sim \pm 2e$, and on the variation of structural distortions, which on the contrary, can be small if the electric field is parallel to the spontaneous polarization (Fig. 6d,f). We then decided to perform a direct calculation of the piezoelectric stress coefficient, firstly in order to confirm this coefficient, which has been calculated by fitting the variation of strain over a wide range of electric field \mathcal{E} , and secondly to verify if the total piezoelectric coefficient, including the purely electronic contribution, is also negative or not. To do so, we applied the DFPT to the *Ima2* structure calculated at $\mathcal{E} = 0$ V m $^{-1}$ and we calculated the piezoelectric stress coefficients $e_{ij} = \frac{\delta P_i}{\delta \eta_j}$. We found ion-clamped terms equal to $\bar{e}_{22} = +15.3$ $\mu\text{C cm}^{-2}$ (in Voigt notations) and $\bar{e}_{23} = -8.7$ $\mu\text{C cm}^{-2}$, which are much smaller than the ionic terms, calculated using finite-difference approach, $e'_{22} = -53.3$ $\mu\text{C m}^{-2}$ and $e'_{23} = 73.2$ $\mu\text{C cm}^{-2}$. This calculation thus confirms that the lattice-mediated contribution to the piezoelectric coefficients dominates and is responsible for a negative total piezoelectric coefficient. From the full set of coefficients e_{ij} , it is possible to calculate the total converse piezoelectric charge coefficients (see Table III in Appendix C) $d_{22} = -2.88$ pm V $^{-1}$ and $d_{23} = 4.58$ pm V $^{-1}$, which are close from the ionic terms d_y and d_z reported in Table II.

IV. CONCLUSION

With our first-principles calculations, we found that the ground state of the brownmillerite oxide Ca $_2$ Al $_2$ O $_5$ corresponds to the non-polar phase of space group *Pbcm*, associated with an antiferroelectric ordering and chains of oxygen tetrahedra having alternatively opposite handednesses along the [100] direction. In addition to this ground state, several other phases with close internal en-

ergies can be formed by changing the distribution of chain handednesses. This richness of phase diagrams mostly comes from the relatively low structural coupling between the different chains. The second most stable phase is calculated to be the ferroelectric *Ima2* phase; this phase was experimentally observed at room temperature, which might be the consequence of the needed high temperature and pressures to grow $\text{Ca}_2\text{Al}_2\text{O}_5$. The calculated electric polarization in $\text{Ca}_2\text{Al}_2\text{O}_5$ is close from the one measured in $\text{Sr}_2\text{Fe}_2\text{O}_5$ [3] and strategies would thus have to be developed in order to make such ferroelectric materials interesting for potential applications. Applying a strain is for example often envisioned to increase the electric polarization, but, as already shown by Young and Rondinelli [5] and by our calculations, the strain response in brownmillerite may be difficult to predict without a thorough study, because of the strong coupling with the tetrahedra tilts.

At low temperature and without any external electric field, it appears that once one of the four considered phases is stabilized, it should remain robust owing to the high energy barrier (in the order of ~ 1 eV per chain of two tetrahedras), which have to be overpassed in order to switch between different phases, by changing one chain handedness. From the calculated barriers, we can conclude that the switching between different phases will generally require to go through intermediate states and to reverse the chain polarization one by one. At this stage, it is not possible to know if these reversals will be random or associated to the displacements of domain boundaries. We however found that the reversal of consecutive chains is slightly easier when the chains are lying in the same (001) atomic layer. In any case, because of the calculated high energy barrier to overpass, we proposed that *Ima2* polar phases could be more easily stabilized by applying an electric field at high temperature and then slowly cooling down the crystal to preserve the phase at room temperature. Such method could provide an additional way to ensure the stabilization of polar phases in brownmillerite structures, in addition to the control of other parameters such as epitaxial strain.

We finally discussed the variation of strain as a function of the external electric field applied along the T chain directions. We found that, due to the electrostrictive behavior, which will change the interlayer distances, or in other words the lattice coupling between the different chains, the electric field could help to stabilize different non-polar phases. When a polar phase is stabilized, we predict that, because of its low lattice response, $\text{Ca}_2\text{Al}_2\text{O}_5$ possesses a negative longitudinal piezoelectric coefficient in the direction parallel to the field.

We chose to focus our study on the non-magnetic $\text{Ca}_2\text{Al}_2\text{O}_5$ brownmillerite. We can expect that the results and mechanisms described in this paper would remain qualitatively valid for other compounds, more suitable for applicative purposes, such as $\text{Sr}_2\text{Fe}_2\text{O}_5$ or $\text{Sr}_2\text{Co}_2\text{O}_5$. Because we found that the energy barrier to transit between different crystallographic phases is of the same or-

der of magnitude than the energy barrier for one oxygen atom to move between two atomic sites [15, 45], it would be interesting to extend the current study in order to try to understand if a coupling can exist between these two processes, to verify if the oxygen conductivity can be facilitated by the stabilization of a particular crystallographic phase or if the mobility of atoms can be concomitant with the switching between different phases. Finally, another continuation to this work would be to investigate the effect of an electric field applied in directions perpendicular to the chains of oxygen tetrahedra, in order to see if it can allow to stabilize new phases or to understand how it could help to rotate the chains direction [7].

ACKNOWLEDGMENTS

This work was granted access to the HPC resources of CALMIP (Allocation No. 2021-2023/P19004). L.B. thanks the support from Vannevar Bush Faculty Fellowship (VBFF) Grant No. N00014-20-1-2834 from the Department of Defense and ONR Grant No. N00014-21-1-2086.

Appendix A: Born effective charges

The Born effective charges Z^* (in e) calculated for every atoms using the centrosymmetric structure *Imma* are:

$$Z^*(\text{Ca}) = \begin{pmatrix} 2.65495 & 0 & 0.01310 \\ 0 & 2.50003 & 0 \\ -0.00592 & 0 & 2.18606 \end{pmatrix}$$

$$Z^*(\text{Al}_T) = \begin{pmatrix} 2.24139 & 0 & 0 \\ 0 & 2.33007 & 0 \\ 0 & 0 & 2.76508 \end{pmatrix}$$

$$Z^*(\text{Al}_O) = \begin{pmatrix} 3.04751 & 0 & 0.07125 \\ 0 & 2.92637 & 0 \\ 0.06968 & 0 & 2.97150 \end{pmatrix}$$

$$Z^*(\text{O}_{\text{Ca}}) = \begin{pmatrix} -1.97569 & 0 & \pm 0.19361 \\ 0 & -1.70541 & 0 \\ \pm 0.17645 & 0 & -2.38144 \end{pmatrix}$$

$$Z^*(\text{O}_{\text{Al}_T}) = \begin{pmatrix} -1.88292 & \pm 0.42739 & 0 \\ \pm 0.48843 & -2.19961 & 0 \\ 0 & 0 & -1.82320 \end{pmatrix}$$

$$Z^*(O_{AlO}) = \begin{pmatrix} -2.37623 & \pm 0.10791 & \pm 0 \\ \pm 0.14031 & -2.31655 & 0 \\ \pm 0 & 0 & -1.75623 \end{pmatrix}$$

Appendix B: Born effective charges

In Fig. 8, we displayed the atomic structures corresponding to the minima and maxima calculated along the $46(-P) \rightarrow 26 \rightarrow 57 \rightarrow 26 \rightarrow 46(+P)$ reaction path. As it can be seen in this figure, the T chain are rotated one by one and the barrier energy maxima correspond to tetrahedra tilts angles $\theta_T = 0^\circ$. Looking more closely at the atomic structure, we can see that the rotation of the tetrahedra induces a small variation of the Al position along the $[010]$ $\delta y(\text{Al})$, while the stronger variation of $\delta y(\text{O})$ is mostly governed by the displacement of the O_2 atoms, which are linking the different tetrahedra of a given chain (see Fig. 8). When $\theta_T = 0^\circ$, the oxygen atoms O_2 are located in between the two Al atoms, which cor-

responds to the maximum of hinder, thus resulting in an increase of the b lattice parameter by 0.04 Å and a local maximum of the energy U along the NEB reaction path.

Appendix C: Piezoelectric coefficients and elastic constants

We performed calculations of the converse piezoelectric coefficients $d_{ij} = \frac{\delta \eta_i}{\delta \mathcal{E}_j}$ and the stress piezoelectric coefficients $e_{ij} = \frac{\delta P_i}{\delta \eta_j}$, which are labeled following Voigt notations [50]. The ion-clamped, \bar{e}_{ij} , and internal-strain terms e'_{ij} , are calculated from the DFPT [47, 48] and finite differences. The d_{ij} coefficients are related to e_{ik} through the elastic compliances S_{kj} [47, 52]:

$$d_{ij} = \frac{\delta P_i}{\delta \eta_j} = e_{ik} (C^{-1})_{kj} = e_{ik} S_{kj} \quad (\text{C1})$$

with C_{kj} being the elastic constants.

The coefficients calculated for the *Ima2* structure are summarized in Table III.

- [1] M. T. Anderson, J. T. Vaughey, and K. R. Poeppelmeier, Structural similarities among oxygen-deficient perovskites, *Chem. Mater.* **5**, 151 (1993).
- [2] J. Young, E. J. Moon, D. Mukherjee, G. Stone, V. Gopalan, N. Alem, S. J. May, and J. M. Rondinelli, Polar oxides without inversion symmetry through vacancy and chemical order, *J. Am. Chem. Soc.* **139**, 2833 (2017).
- [3] K. T. Kang, C. J. Roh, J. Lim, T. Min, J. H. Lee, K. Lee, T. Y. Lee, S. Kang, D. Seol, J. Kim, H. Ohta, A. Khare, S. Park, Y. Kim, S. C. Chae, Y. S. Oh, J. Lee, J. Yu, J. S. Lee, and W. S. Choi, A room-temperature ferroelectric ferromagnet in a 1D tetrahedral chain network, *Adv. Mater.* **31**, 1808104 (2019).
- [4] H. Tian, L. Bellaiche, and Y. Yang, Diversity of structural phases and resulting control of properties in brownmillerite oxides: A first-principles study, *Phys. Rev. B* **100**, 220103(R) (2019).
- [5] J. Young and J. M. Rondinelli, Crystal structure and electronic properties of bulk and thin film brownmillerite oxides, *Phys. Rev. B* **92**, 174111 (2015).
- [6] A. Khare, J. Lee, J. Park, G.-Y. Kim, S.-Y. Choi, T. Katase, S. Roh, T. S. Yoo, J. Hwang, H. Ohta, J. Son, and W. S. Choi, Directing oxygen vacancy channels in $\text{SrFeO}_{2.5}$ epitaxial thin films, *ACS Appl. Mater. Interfaces* **10**, 4831 (2018).
- [7] L. Zhu, L. Gao, L. Wang, Z. Xu, J. Wang, X. Li, L. Liao, T. Huang, H. Huang, A. Ji, N. Lu, Z. Cao, Q. Li, J.-R. Sun, P. Yu, and X. Bai, Atomic-scale observation of structure transition from brownmillerite to infinite layer in $\text{SrFeO}_{2.5}$ thin films, *Chem. Mater.* **33**, 3113 (2021).
- [8] H. Han, A. Sharma, H. L. Meyerheim, J. Yoon, H. Deniz, K.-R. Jeon, A. K. Sharma, K. Mohseni, C. Guillemond, M. Valvidares, P. Gargiani, and S. S. P. Parkin, Control

TABLE III. Stress piezoelectric coefficients e_{ij} and converse piezoelectric coefficients d_{ij} calculated directly from DFT, for the ferroelectric phase *Ima2*. The coefficients are given in Voigt notations [50].

ij	\bar{e}_{ij}	e'_{ij}	d_{ij}
	$\mu\text{C cm}^{-2}$	$\mu\text{C cm}^{-2}$	pm V^{-1}
21	-7.8	27.4	-0.899
22	15.3	-53.3	-2.883
23	-8.7	73.2	4.577
35	-7.5	48.2	4.504
16	-7.0	13.9	0.987

- of oxygen vacancy ordering in brownmillerite thin films via ionic liquid gating, *ACS Nano* **16**, 6206 (2022).
- [9] M. A. Hayward and M. J. Rosseinsky, Cool conditions for mobile ions, *Nature* **450**, 960 (2007).
- [10] W. Paulus, H. Schober, S. Eibl, M. Johnson, T. Berthier, O. Hernandez, M. Ceretti, M. Plazanet, K. Conder, and C. Lamberti, Lattice dynamics to trigger low temperature oxygen mobility in solid oxide ion conductors, *J. Am. Chem. Soc.* **130**, 16080 (2008).
- [11] H. Jeon, W. S. Choi, J. W. Freeland, H. Ohta, C. U. Jung, and H. N. Lee, Topotactic phase transformation of the brownmillerite $\text{SrCoO}_{2.5}$ to the perovskite $\text{SrCoO}_{3-\delta}$, *Adv. Mater.* **25**, 3651 (2013).
- [12] V. R. Nallagatla, T. Heisig, C. Baeumer, V. Feyer, M. Jugovac, G. Zamborlini, C. M. Schneider, R. Waser, M. Kim, C. U. Jung, and R. Dittmann, Topotactic phase transition driving memristive behavior, *Adv. Mater.* **31**, 1903391 (2019).

- [13] J. Tian, H. Wu, Z. Fan, Y. Zhang, S. J. Pennycook, D. Zheng, Z. Tan, H. Guo, P. Yu, X. Lu, G. Zhou, X. Gao, and J.-M. Liu, Nanoscale topotactic phase transformation in SrFeO_x epitaxial thin films for high-density resistive switching memory, *Adv. Mater.* **31**, 1903679 (2019).
- [14] M. S. Saleem, B. Cui, C. Song, Y. Sun, Y. Gu, R. Zhang, M. U. Fayaz, X. Zhou, P. Werner, S. S. P. Parkin, and F. Pan, Electric field control of phase transition and tunable resistive switching in SrFeO_{2.5}, *ACS Appl. Mater. Interfaces* **11**, 6581 (2019).
- [15] X. Mou, J. Tang, Y. Lyu, Q. Zhang, S. Yang, F. Xu, W. Liu, M. Xu, Y. Zhou, W. Sun, Y. Zhong, B. Gao, P. Yu, H. Qian, and H. Wu, Analog memristive synapse based on topotactic phase transition for high-performance neuromorphic computing and neural network pruning, *Science Advances* **7**, eabh0648 (2021).
- [16] T. G. Parsons, H. D'Hondt, J. Hadermann, and M. A. Hayward, Synthesis and structural characterization of La_{1-x}A_xMnO_{2.5} (A = Ba, Sr, Ca) phases: Mapping the variants of the Brownmillerite structure, *Chem. Mater.* **21**, 5527 (2009).
- [17] H. Tian, X.-Y. Kuang, A.-J. Mao, Y. Yang, H. Xiang, C. Xu, S. O. Sayedaghaee, J. Íñiguez, and L. Bellaiche, Novel type of ferroelectricity in brownmillerite structures: A first-principles study, *Phys. Rev. Materials* **2**, 084402 (2018).
- [18] A. P. Levanyuk and D. G. Sannikov, Improper ferroelectrics, *Sov. Phys. Usp.* **17**, 199 (1974).
- [19] E. Bousquet, M. Dawber, N. Stucki, C. Lichtensteiger, P. Hermet, S. Gariglio, J.-M. Triscone, and P. Ghosez, Improper ferroelectricity in perovskite oxide artificial superlattices, *Nature* **452**, 732 (2008).
- [20] N. A. Benedek and C. J. Fennie, Hybrid improper ferroelectricity: A mechanism for controllable polarization-magnetization coupling, *Phys. Rev. Lett.* **106**, 107204 (2011).
- [21] A. T. Mulder, N. A. Benedek, J. M. Rondinelli, and C. J. Fennie, Turning ABO₃ antiferroelectrics into ferroelectrics: Design rules for practical rotation-driven ferroelectricity in double perovskites and A₃B₂O₇ Ruddlesden-Popper compounds, *Adv. Funct. Mater.* **23**, 4810.
- [22] H. J. Zhao, J. Íñiguez, W. Ren, X. M. Chen, and L. Bellaiche, Atomistic theory of hybrid improper ferroelectricity in perovskites, *Phys. Rev. B* **89**, 174101 (2014).
- [23] J. Holakovský, A new type of the ferroelectric phase transition, *Phys. Status Solidi (b)* **56**, 615 (1973).
- [24] I. A. Kornev and L. Bellaiche, Nature of the ferroelectric phase transition in multiferroic BiFeO₃ from first principles, *Phys. Rev. B* **79**, 100105(R) (2009).
- [25] A. M. Abakumov, A. S. Kalyuzhnaya, M. G. Rozova, E. V. Antipov, J. Hadermann, and G. Van Tendeloo, Compositionally induced phase transition in the Ca₂MnGa_{1-x}Al_xO₅ solid solutions: Ordering of tetrahedral chains in brownmillerite structure, *Solid State Sci.* **7**, 801 (2005).
- [26] J. Hadermann, A. M. Abakumov, H. D'Hondt, A. S. Kalyuzhnaya, M. G. Rozova, M. M. Markina, M. G. Mikheev, N. Tristan, R. Klingeler, B. Büchner, and E. V. Antipov, Synthesis and crystal structure of the Sr₂Al_{1.07}Mn_{0.93}O₅ brownmillerite, *J. Mater. Chem.* **17**, 692 (2007).
- [27] S. Lambert, H. Leligny, D. Grebille, D. Pelloquin, and B. Raveau, Modulated distribution of differently ordered tetrahedral chains in the brownmillerite structure, *Chem. Mater.* **14**, 1818 (2002).
- [28] H. Krüger and V. Kahlenberg, Incommensurately modulated ordering of tetrahedral chains in Ca₂Fe₂O₅ at elevated temperatures – structure investigation and Raman spectroscopy, *Acta Crystallogr. Sect. B* **61**, 656 (2005).
- [29] B. Lazic, H. Krüger, V. Kahlenberg, J. Konzett, and R. Kaindl, Incommensurate structure of Ca₂Al₂O₅ at high temperatures – structure investigation and Raman spectroscopy, *Acta Crystallogr. Sect. B* **64**, 417 (2008).
- [30] H. Fu and L. Bellaiche, First-principles determination of electromechanical responses of solids under finite electric fields, *Phys. Rev. Lett.* **91**, 057601 (2003).
- [31] P. Hohenberg and W. Kohn, Inhomogeneous electron gas, *Phys. Rev.* **136**, B864 (1964).
- [32] W. Kohn and L. J. Sham, Self-consistent equations including exchange and correlation effects, *Phys. Rev.* **140**, A1133 (1965).
- [33] G. Kresse and J. Hafner, Ab initio molecular-dynamics simulation of the liquid-metal–amorphous-semiconductor transition in germanium, *Phys. Rev. B* **49**, 14251 (1994).
- [34] G. Kresse and J. Furthmüller, Efficient iterative schemes for ab initio total-energy calculations using a plane-wave basis set, *Phys. Rev. B* **54**, 11169 (1996).
- [35] P. E. Blöchl, Projector augmented-wave method, *Phys. Rev. B* **50**, 17953 (1994).
- [36] J. P. Perdew, A. Ruzsinszky, G. I. Csonka, O. A. Vydrov, G. E. Scuseria, L. A. Constantin, X. Zhou, and K. Burke, Restoring the density-gradient expansion for exchange in solids and surfaces, *Phys. Rev. Lett.* **100**, 136406 (2008); Erratum: Restoring the density-gradient expansion for exchange in solids and surfaces [*phys. rev. lett.* **100**, 136406 (2008)], *Phys. Rev. Lett.* **102**, 039902(E) (2009).
- [37] H. J. Monkhorst and J. D. Pack, Special points for Brillouin-zone integrations, *Phys. Rev. B* **13**, 5188 (1976).
- [38] G. Henkelman, B. P. Uberuaga, and H. Jónsson, A climbing image nudged elastic band method for finding saddle points and minimum energy paths, *J. Chem. Phys.* **113**, 9901 (2000).
- [39] P. Aggarwal, J. Gard, F. Glasser, and G. Biggar, Synthesis and properties of dicalcium aluminate, 2CaO·Al₂O₃, *Cem. Concr. Res* **2**, 291 (1972).
- [40] V. Kahlenberg, R. X. Fischer, and C. S. J. Shaw, Rietveld analysis of dicalcium aluminate (Ca₂Al₂O₅) – A new high pressure phase with the Brownmillerite-type structure, *Am. Mineral.* **85**, 1061 (2000).
- [41] G. Hentschel, Mayenit, 12CaO·7Al₂O₃, und brownmillerit, 2CaO·(Al,Fe)₂O₃, zwei neue Minerale in den Kalksteinschlüssen der Lava des Ettringer Bellerberges, *Neues Jahrb. für Mineral. Monatshefte* **1964**, 22 (1964).
- [42] H. Taylor, *Cement chemistry, 2nd ed.* (Thomas Telford Publishing, 1997).
- [43] G. J. Redhammer, T. G., G. Roth, and G. Amthauer, Structural variations in the brownmillerite series Ca₂(Fe_{2-x}Al_x)O₅: Single-crystal x-ray diffraction at 25 °C and high-temperature x-ray powder diffraction (25 °C ≤ T ≤ 1000 °C), *Am. Mineral.* **89**, 405 (2004).
- [44] X. Y. Li, Q. Yang, J. X. Cao, L. Z. Sun, Q. X. Peng, Y. C. Zhou, and R. X. Zhang, Domain wall motion in perovskite ferroelectrics studied by the nudged elastic band method, *J. Phys. Chem. C* **122**, 3091 (2018).
- [45] U. Matsumoto, A. Kuwabara, C. A. J. Fisher,

- 1016 H. Moriwake, and I. Tanaka, Oxide-ion diffusion in 1035
 1017 brownmillerite-type $\text{Ca}_2\text{AlMnO}_{5+\delta}$ from first-principles 1036
 1018 calculations, *Phys. Chem. Chem. Phys.* **24**, 1503 (2022). 1037
- 1019 [46] D.-H. Choe, S. Kim, T. Moon, S. Jo, H. Bae, S.-G. Nam, 1038
 1020 Y. S. Lee, and J. Heo, Unexpectedly low barrier of ferro- 1039
 1021 electric switching in HfO_2 via topological domain walls, 1040
 1022 *Mat. Today* **50**, 8 (2021). 1041
- 1023 [47] X. Wu, D. Vanderbilt, and D. R. Hamann, Systematic 1042
 1024 treatment of displacements, strains, and electric fields in 1043
 1025 density-functional perturbation theory, *Phys. Rev. B* **72**, 1044
 1026 035105 (2005). 1045
- 1027 [48] M. Gajdoš, K. Hummer, G. Kresse, J. Furthmüller, and 1046
 1028 F. Bechstedt, Linear optical properties in the projector- 1047
 1029 augmented wave methodology, *Phys. Rev. B* **73**, 045112 1048
 1030 (2006). 1049
- 1031 [49] D. S. P. Tanner, E. Bousquet, and P.-E. Janolin, Opti- 1050
 1032 mized methodology for the calculation of electrostriction 1051
 1033 from first-principles, *Small* **17**, 2103419 (2021).
- 1034 [50] J. F. Nye, *Physical properties of crystals: Their repre-
 sentation by tensors and matrices* (Oxford Science Pub-
 lications, Clarendon Press, 1985).
- [51] K. S. Suzuki and H. O. H. Okumura, First-principles
 study on piezoelectric constants in strained BN, AlN, and
 GaN, *Jpn. J. Appl. Phys.* **37**, L1421 (1998).
- [52] S. Dutta, P. Buragohain, S. Glinsek, C. Richter,
 H. Aramberri, H. Lu, U. Schroeder, E. Defay, A. Gruver-
 man, and J. Íñiguez, Piezoelectricity in hafnia, *Nature*
Commun. **12**, 7301 (2021).
- [53] S. Liu and R. E. Cohen, Origin of negative longitudinal
 piezoelectric effect, *Phys. Rev. Lett.* **119**, 207601 (2017).
- [54] Y. Qi and A. M. Rappe, Widespread negative longitudi-
 nal piezoelectric responses in ferroelectric crystals with
 layered structures, *Phys. Rev. Lett.* **126**, 217601 (2021).
- [55] G. Sághi-Szabó, R. E. Cohen, and H. Krakauer, First-
 principles study of piezoelectricity in PbTiO_3 , *Phys. Rev.*
Lett. **80**, 4321 (1998).

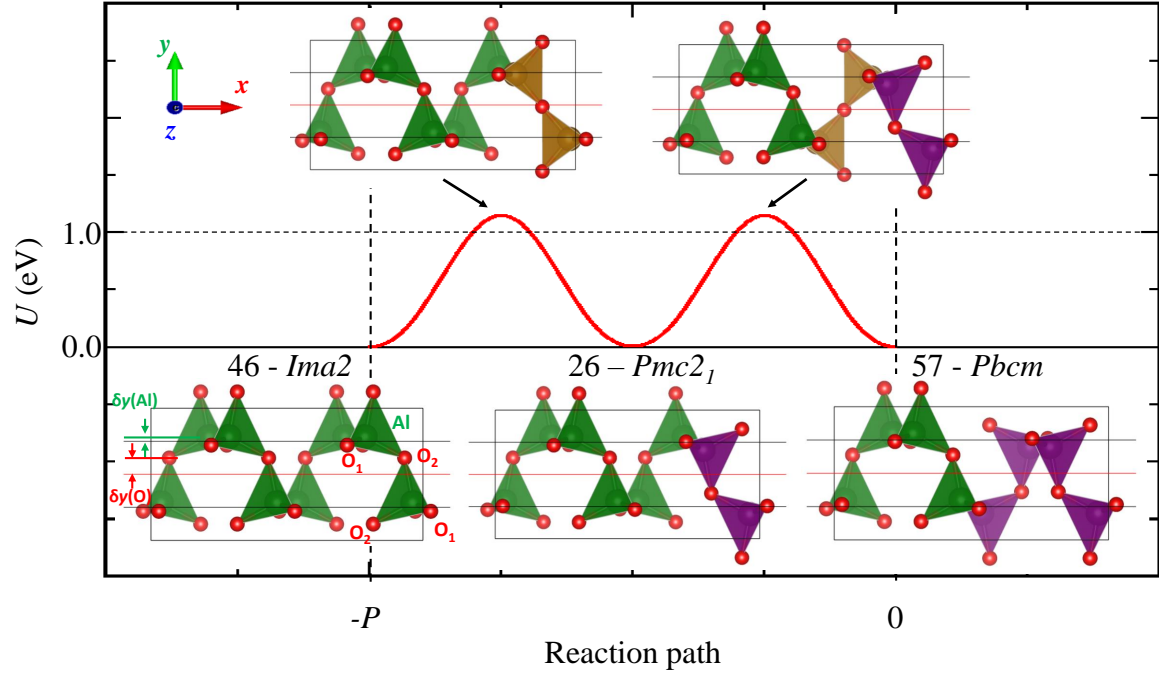


FIG. 8. Atomic structures [projected on a (001) plane] calculated with the NEB method for the $46(-P) \rightarrow 26 \rightarrow 57 \rightarrow 26 \rightarrow 46(+P)$ reaction path given in Fig. 2. Only half of the reaction path is shown as it is symmetrical when no electric field is applied.